Research
Advanced Materials and Materials Genome—Article

Thermal and Mechanical Properties Optimization of ABO_4 Type $EuNbO_4$ By the B-Site Substitution of Ta

Lin Chen, Jing Feng *

Faculty of Material Science and Engineering, Kunming University of Science and Technology, Kunming 650093, China

ARTICLE INFO

ABSTRACT

Ferroelastic ABO_4 type $RETaO_4$ and $RENbO_4$ ceramics (where RE stands for rare earth) are being investigated as promising thermal barrier coatings (TBCs), and the mechanical properties of $RETaO_4$ have been found to be better than those of $RENbO_4$. In this work, B-site substitution of tantalum (Ta) is used to optimize the thermal and mechanical properties of $EuNbO_4$ fabricated through a solid-state reaction (SSR). The crystal structure is clarified by means of X-ray diffraction (XRD) and Raman spectroscopy; and the surface microstructure is surveyed via scanning electronic microscope (SEM). The Young's modulus and the thermal expansion coefficient (TEC) of $EuNbO_4$ are effectively increased; with respective maximum values of 169 GPa and 11.2×10^{-6} K^{-1} (at 1200 °C). The thermal conductivity is reduced to 1.52 $W \cdot K^{-1} \cdot m^{-1}$ (at 700 °C), and the thermal radiation resistance is improved. The relationship between the phonon thermal diffusivity and temperature was established in order to determine the intrinsic phonon thermal conductivity by eliminating the thermal radiation effects. The results indicate that the thermal and mechanical properties of $EuNbO_4$ can be effectually optimized via the B-site substitution of Ta, and that this proposed material can be applied as a high-temperature structural ceramic in future.

© 2020 THE AUTHORS. Published by Elsevier LTD on behalf of Chinese Academy of Engineering and Higher Education Press Limited Company. This is an open access article under the CC BY-NC-ND license (http://creativecommons.org/licenses/by-nc-nd/4.0/).

1. Introduction

Ferroelastic rare earth tantalates and niobates ($RETaO_4$ and $RENbO_4$, where RE stands for rare earth) are being researched for diverse applications, according to their individual properties [1–5]. The investigative fields of $RENbO_4$ include proton-conducting solid oxide fuel cells, microwave dielectric materials, and shape memory materials [5–8]. The prominent properties of rare earth niobates come from their distinctive crystal structure and the various ligands of niobium (Nb). The crystal structure of $RENbO_4$ is dominated by Nb, and $RENbO_4$ undergoes a reversible ferroelastic crystal structure transformation with variation of temperature [2,4,5]. At high temperatures, $RENbO_4$ is in a tetragonal (t) phase, which transforms to a monoclinic (m) phase at room temperature [2,5]. The t–m transformation temperature of $RENbO_4$ is between 500 and 800 °C, depending on the rare earth elements [2,5]. Usually, an evident change in unit cell volume is detected during crystal structure transformation; however, such change is not found in $RENbO_4$ and $RETaO_4$ [2,4,5,8]. Current documents prove that the ferroelastic t–m transformation of $RENbO_4$ and

$RETaO_4$ is a natural second-order transition; no atomic rearrangement is detected. Therefore, volume variation in $RENbO_4$ and $RETaO_4$, that is caused by t–m transformation is neglected.

$RETaO_4$ exhibits a crystal structure that is analogous to that of $RENbO_4$. Different crystal structures are found in $RETaO_4$, which is ascribed to decrease in RE^{3+} ionic radius. $RETaO_4$ (where RE = Y, Nd–Er) has the m phase, while the rest have the metastable monoclinic (m') phase [1,8]. Furthermore, $RETaO_4$ exhibits a much higher t–m transition temperature than $RENbO_4$. For example, the transition temperature of $YTaO_4$ is about 1430 °C, while it is less than 800 °C for $RENbO_4$ [2,8]. Ferroelastic toughness is a critical property that allows 6 wt%–8 wt% yttria-stabilized zirconia (6–8YSZ) to be applied as a thermal barrier coating (TBC) [9–12]. However, the working temperature limit of yttria-stabilized zirconia (YSZ) is below 1200 °C because of phase transition, which results in a huge volume change. Much effort has been devoted to optimizing the properties of YSZ, and many materials are being investigated as TBCs [13–19]. Herein, ferroelastic $RETaO_4$ and $RENbO_4$ are studied as TBCs with a higher application temperature to replace 6–8YSZ. $RETaO_4$ possesses better thermal and mechanical properties than $RENbO_4$, due to the characteristic properties of tantalum (Ta). In addition, the weak bonding strength of $RENbO_4$ produces an inferior hardness and Young's modulus, which makes

---

it less useful for application as high-temperature TBCs. Nevertheless, lower centrifugal force will be produced when $RENbO_4$ is applied as TBCs in comparison with $RETaO_4$, due to the lower density. To modify the properties of $RENbO_4$, the B-site substitution of Ta is attempted for $EuNbO_4$ by applying the atomic weight misfit between Ta and Nb and the difference in bond strength between the Ta–O and Nb–O bonds.

In this paper, $EuNb_{1-X}Ta_XO_4$ (composition parameter X = 0/6, 1/6, 2/6, 3/6, 4/6) specimens were fabricated via a solid-state reaction (SSR). The crystal structure was clarified by means of X-ray diffraction (XRD) and Raman spectra. The surface grain size, pores, and cracks were surveyed by means of scanning electronic microscope (SEM). The thermal and mechanical properties (i.e., heat capacity, thermal diffusivity and conductivity, thermal radiation resistance, thermal expansion performance, inharmonic lattice vibration strength, and Young's modulus) were modified by the B-site substitution of Ta. This work stresses that $EuNbO_4$ ceramics are promising TBCs via further property optimization.

2. Experimental process

The $EuNb_{1-X}Ta_XO_4$ (X = 0/6, 1/6, 2/6, 3/6, 4/6) bulk specimens were synthesized by SSR. Crude substances included Eu_2O_3, Ta_2O_5, and Nb_2O_5 powders and C_2H_5OH (Shanghai Aladdin Bio-Chem Technology Co., Ltd., China). The weighted substance was ball-milled (720 min, 240 r·min^{-1}) within C_2H_5OH. The mixture was kept at 90 °C for 840 min to eliminate C_2H_5OH. The arid mixtures were pressed into a bulk with a radius of 7.5 mm and a thickness of 2 mm. Before sintering, the bulk samples were held at 280 MPa for 8 min, they were then sintered at 1400–1600 °C for 10 h to obtain dense samples.

The crystal structure was confirmed by means of XRD (MiniFlex600, Rigaku Corporation, Japan). Raman spectroscopy was employed to research the change in crystal structure, along with XRD. A confocal spectrometer (Horiba–Jobin Yvon, Horiba, Ltd., USA) was utilized to collect Raman spectra using a He–Ne ion laser (532 nm). SEM (EVO 180, Zeiss, Germany) was employed to survey the superficial morphology, because the grain size, pores, and cracks affected the thermal and mechanical properties.

The longitudinal (V_L) and transverse (V_T) acoustic velocities of $EuNb_{1-X}Ta_XO_4$ were calculated by determining the transmission interval through an ultrasonic pulser/receiver instrument (UMS–100, TECLAB, France). Various properties were identified [20]:

$$\text{Mean acoustic velocity: } V_M = \left[\frac{1}{3}\left(\frac{1}{V_L^3}+\frac{2}{V_T^3}\right)\right]^{-\frac{1}{3}} \qquad (1)$$

$$\text{Young's modulus: } E = \frac{\rho V_T^2\left(3V_L^2-4V_T^2\right)}{V_L^2-V_T^2} \qquad (2)$$

$$\text{Poissons ratio: } v = \frac{1-2(V_T/V_L)^2}{2-2(V_T/V_L)^2} \qquad (3)$$

$$\text{Shear modulus: } G = \frac{E}{2(1+v)} \qquad (4)$$

$$\text{Bulk modulus: } B = \frac{E}{3(1-2v)} \qquad (5)$$

$$\text{Gruneisen parameter: } \gamma = \frac{3}{2}\left(\frac{1+v}{2-3v}\right) \qquad (6)$$

The thermal expansion coefficients (TECs) were determined by means of a thermal expansion rate curve. Thermo–mechanical

analysis (TMA 402 F3, NETZSCH, Germany) was employed to test the temperature-dependent thermal expansion rate (100–1200 °C). The test was conducted in argon (Ar) gaseous fluid, the specimens were cut to a size of 8 mm × 2 mm × 1 mm to adapt to the sample holder. The heating speed was 5 K·min^{-1}. The test time lasted for about 5 h, with only one sample being tested each time.

The bulk specimens were machined into discs with a radius of 3 mm and a thickness of 1 mm to fit the sample holder in order to test the thermal diffusivity (λ). Silver (Ag) and carbon (C) coatings were applied to reduce the thermal radiative conductivity, and ensure to absorption and maximum emissivity. The test was executed under Ar gas protection within a laser flash instrument (LFA 457, NETZSCH, Germany). Three samples were tested each time, and the test lasted for about 12 h. The thermal diffusivity was corrected by means of the "radiation + pulse" method; three tests were performed at each temperature point and the average value was used. The thermal conductivity (k') was determined from the λ, C_P, and ρ as follows [21]:

$$k' = \lambda C_P \rho \qquad (7)$$

where the specific heat, C_p, was computed using the Neumann–Kopp principle [22], and ρ is the density. The influence of porosity, ϕ, on thermal conductivity was removed as follows [21]:

$$\frac{k'}{k} = 1 - \frac{4}{3}\phi \qquad (8)$$

Debye's principle was employed to investigate the thermal conduction mechanism. The thermal conduction mechanism was related to the propagation of phonons, as heat is transmitted via the phonons in insulators [23]:

$$k = C_V l V_M/3 \qquad (9)$$

where k is the thermal conductivity of fully dense sample, C_V refers to the specific heat per unit volume, and l refers to the phonon mean free path. The influence of the specific heat on thermal conduction was restricted, as it reached $3k_B$ (where k_B is the Boltzmann constant) per atom at high temperatures. Herein, l was obtained:

$$l = 3\lambda/V_M \qquad (10)$$

The phonon mean free path, l, was typically depressed by diverse scattering procedures, indicating that l and k decrease with an increase in the phonon scattering strength.

3. Results and discussion

Fig. 1(a) shows that the experimental $EuNb_{1-X}Ta_XO_4$ XRD peaks are consistent with those of standard PDF#22-1099, and that no peak for the precipitated phase is present. $EuNb_{1-X}Ta_XO_4$ crystallizes in the m phase; no crystal structure transition was detected with an increase in the Ta content. Fig. 1(b) shows that the main XRD peaks slightly deviate from those on the standard PDF card, which relates to the sintering temperature. The final sintering temperature of $EuNbO_4$ is 1400 °C; it increases with an increase in Ta content, and is 1600 °C for $EuNb_{2/6}Ta_{4/6}O_4$. Similar room-temperature Raman peaks were found for $EuNb_{1-X}Ta_XO_4$, as displayed in Fig. 1(c). The shift and intensity of each Raman vibration mode are connected to the molecular vibration and bond length. No evident peak deviation was observed in the two strongest Raman vibration modes (V_1 and V_2) of $EuNb_{1-X}Ta_XO_4$. The results of the Raman spectra align with the situation indicated by XRD; that is no phase transition is detected, indicating that each sample crystallizes in the same m phase.

Fig. 2 shows that the grain size of $EuNb_{1-X}Ta_XO_4$ is less than 20 μm; the $EuNb_{2/6}Ta_{4/6}O_4$ displays a minimal grain size, which
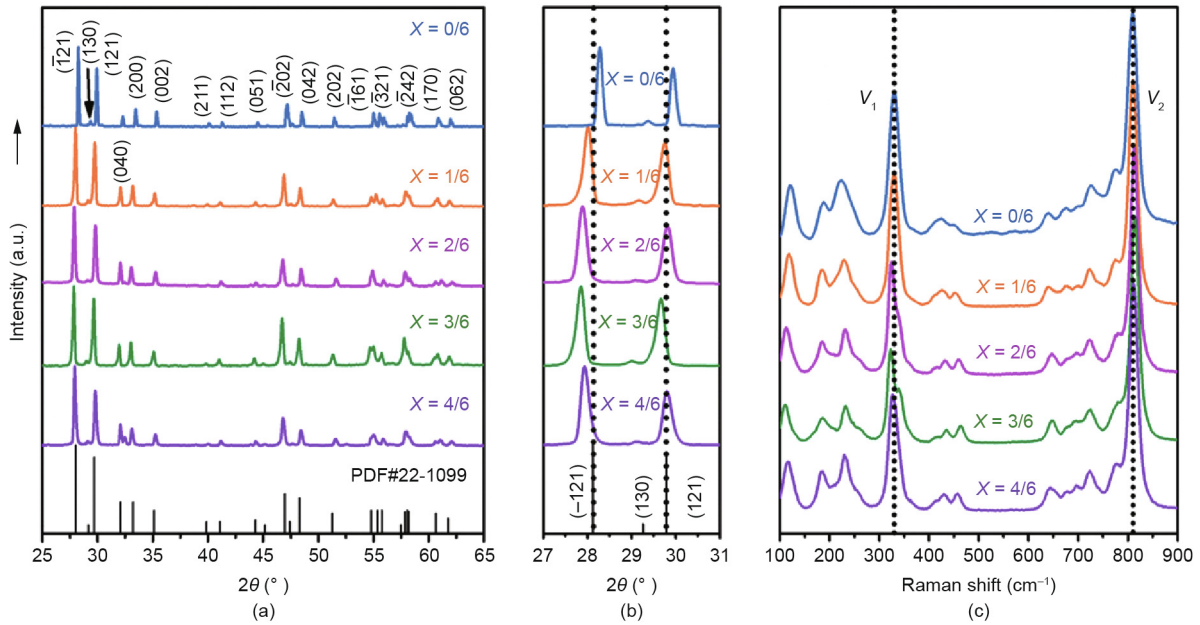
Fig. 1. Phase characterization of $EuNb_{1-X}Ta_XO_4$ (X = 0/6, 1/6, 2/6, 3/6, 4/6) ceramics. (a) XRD, $25° \leq 2\theta \leq 65°$; (b) XRD, $27° \leq 2\theta \leq 31°$; (c) room-temperature Raman spectra (25 °C, 532 nm, 100–900 cm^{-1}).

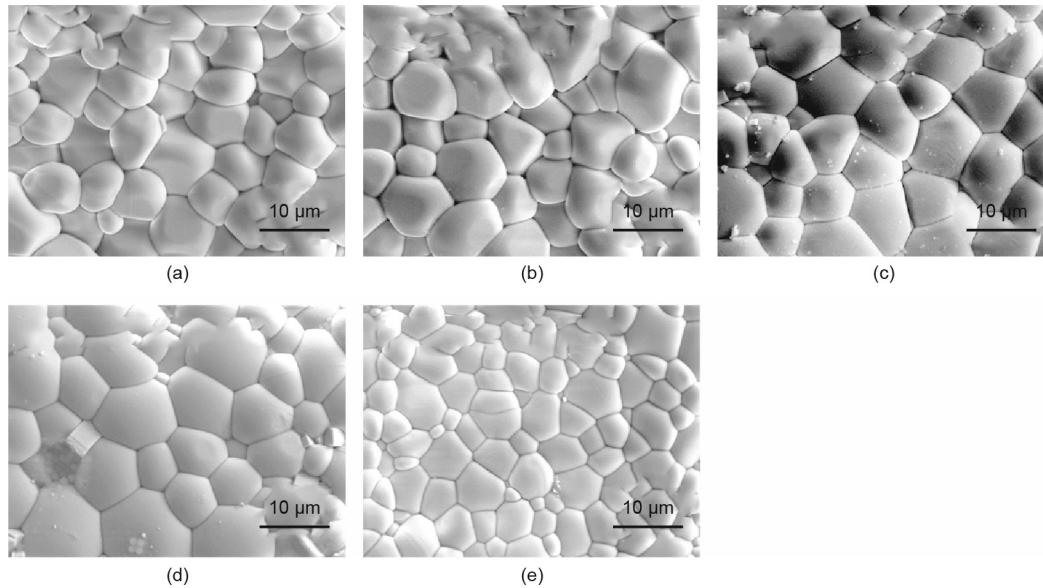**Fig. 2.** Typical surface morphology of $EuNb_{1-X}Ta_XO_4$ (X = 0/6, 1/6, 2/6, 3/6, 4/6) ceramics. (a) $EuNbO_4$; (b) $EuNb_{5/6}Ta_{1/6}O_4$; (c) $EuNb_{4/6}Ta_{2/6}O_4$; (d) $EuNb_{3/6}Ta_{3/6}O_4$; (e) $EuNb_{2/6}Ta_{4/6}O_4$.

is ascribed to the highest sintering temperature. The final sintering temperature is related to the melting point. The final sintering temperature of $EuNbO_4$ is 1400 °C, and the substance melts at 1600 °C. The final sintering temperature of $EuNb_{2/6}Ta_{4/6}O_4$ is 1600 °C; the melting point of $EuNbO_4$ has been increased via the *B*-site substitution of Ta. A higher melting point implies a higher limit application temperature. The grain boundaries are evident, and the grains bond well with each other. The fine grain size and outstanding combination of grains contribute to produce extraordinary thermal and mechanical properties.

The data presented in Table 1 implies that the *B*-site substitution of Ta makes a notable difference to the mechanical properties of $EuNbO_4$. The Young's modulus of $EuNbO_4$ is about 76 GPa, so the *B*-site substitution of Ta has led to an increase in the Young's

modulus. The highest Young's modulus (169 GPa) is detected in $EuNb_{2/6}Ta_{4/6}O_4$. A similar situation is observed in the bulk modulus, shear modulus, and mean acoustic velocity. The composition dependence of the elastic modulus and acoustic velocity of $EuNb_{1-X}Ta_XO_4$ is depicted in Fig. 3. When $X \leq 3/6$, the increase in the elastic modulus and acoustic velocity of $EuNb_{1-X}Ta_XO_4$ is minute. The Young's modulus mirrors the bond strength of the chemical bonds. It is clear that the *B*-site substitution of Ta leads to an increase in the bonding strength. A high Young's modulus means that $EuNb_{1-X}Ta_XO_4$ can be directly applied as high-temperature structural ceramics.

The bond strength increases with a decrease in bond length [24]. Fig. 1 implies that the lattice parameters and unit cell volume of $EuNb_{1-X}Ta_XO_4$ increase with an increase in Ta content, which

Table 1
The mean acoustic velocity, elastic modulus (*E, B, and G*), Grüneisen parameter (*γ*), and Poisson's ratio (*v*) of $EuNb_{1-X}Ta_XO_4$ (*X* = 0/6, 1/6, 2/6, 3/6, 4/6) ceramics.

| X	V_M (m·s^{-1})	E (GPa)	B (GPa)	G (GPa)	γ	v
0/6	2246	76	53	30	1.54	0.26
1/6	2325	95	113	35	2.21	0.36
2/6	2314	92	127	33	2.40	0.38
3/6	2393	102	100	38	1.98	0.33
4/6	3022	169	122	66	1.60	0.27
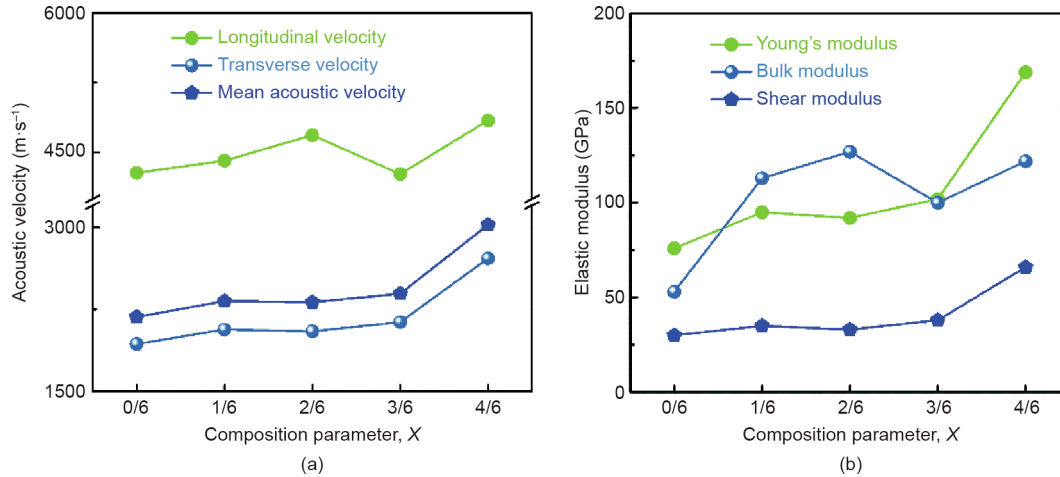
Fig. 3. Composition-dependent acoustic velocity and elastic modulus of $EuNb_{1-X}Ta_XO_4$ (*X* = 0/6, 1/6, 2/6, 3/6, 4/6) ceramics. (a) Acoustic velocity; (b) elastic modulus.

leads to an increase in bond length. Therefore, it is believed that the Ta–O bond strength is much greater than that of the Nb–O bond, which results in an increase of the Young's modulus. Greater bond strength leads to a faster phonon propagation speed, which results in an increase of the thermal conductivity, to a certain extent. However, the factors affecting thermal conduction are complex, and will be discussed in detail.

Fig. 4(a) shows that the thermal expansion rate of $EuNb_{1-X}Ta_XO_4$ rapidly increases with an increase in temperature. At 1200 °C, $EuNbO_4$ exhibits the lowest thermal expansion rate, while $EuNb_{3/6}Ta_{3/6}O_4$ displays the maximal value. Fig. 4(b) shows that $EuNbO_4$ exhibits the lowest TEC (10.2×10^{-6} K^{-1}, 1200 °C), and the TEC of $EuNbO_4$ can be increased by the *B*-site substitution of Ta. The maximal TEC (11.2×10^{-6} K^{-1}, 1200 °C) was obtained for $EuNb_{3/6}Ta_{3/6}O_4$, this value is much higher than that of 7YSZ (10.0×10^{-6} K^{-1}) and $RE_2Zr_2O_7$ (9.0×10^{-6} K^{-1}) [25–27]. A High

TEC will contribute to reducing the thermal stress between topcoat ceramics and substrate alloys during operation, and will prolong the lifetime of the TBC. The crystal structure is relaxed via substitution, leading to an increase in TEC. Nevertheless, the TEC (11.0×10^{-6} K^{-1}) of $EuNb_{2/6}Ta_{4/6}O_4$ is slightly lower than that of $EuNb_{3/6}Ta_{3/6}O_4$, which can be explained by the dramatic increase in the Young's modulus. The difference in Young's modulus between $EuNbO_4$ and $EuNb_{3/6}Ta_{3/6}O_4$ (26 GPa) is much less than that between $EuNb_{3/6}Ta_{3/6}O_4$ and $EuNb_{2/6}Ta_{4/6}O_4$ (67 GPa). When $X \leq 3/6$, the increase in the TECs of $EuNb_{1-X}Ta_XO_4$ is dominated by crystal structure relaxation, as the Young's modulus variation is minute. The TEC of $EuNb_{2/6}Ta_{4/6}O_4$ is higher than that of $EuNbO_4$, and lower than that of $EuNb_{3/6}Ta_{3/6}O_4$. The increasing bonding strength will lead to a decrease in the TEC, to some extent, when $X \geq 4/6$. Thermal expansion of inorganic ceramics stems from inharmonic atomic vibration around the equilibrium position,
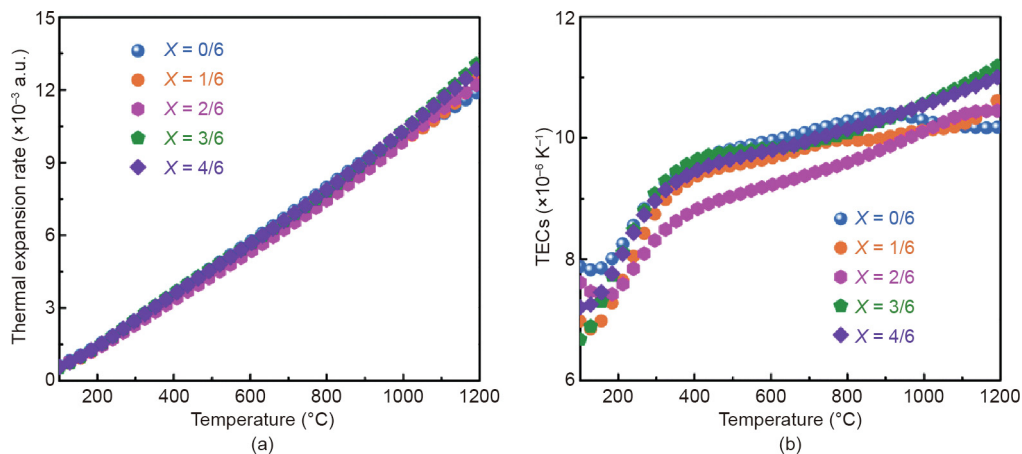
Fig. 4. Thermal expansion performance of $EuNb_{1-X}Ta_XO_4$ (*X* = 0/6, 1/6, 2/6, 3/6, 4/6) ceramics. (a) Thermal expansion rate; (b) TECs.

which is characterized by the Grüneisen parameter. As shown in Table 1, the Grüneisen parameter of EuNbO$_4$ has been increased by the B-site substitution of Ta, which agrees well with the composition-dependent TEC. Thus, it is believed that the TECs of EuNb$_{1-X}$Ta$_X$O$_4$ are governed by different factors with the variation of Ta content.

As shown in Table 2, the specific heat of EuNb$_{1-X}$Ta$_X$O$_4$ increases with an increase in temperature (0.35–0.58 J·K^{-1}·g^{-1}, 25–900 °C). Furthermore, the specific heat of EuNb$_{1-X}$Ta$_X$O$_4$ decreases with an increase in Ta concentration. The specific heat decreases with increasing molecular weight, according to the Neumann–Kopp principle. Fig. 5(a) shows that the thermal diffusivity (0.42–1.13 mm^2·s^{-1}, 25–900 °C) of EuNb$_{1-X}$Ta$_X$O$_4$ quickly decreases with increase in temperature, the lowest thermal diffusivity (0.42–0.90 mm^2·s^{-1}, 25–900 °C) is detected in EuNb$_{3/6}$Ta$_{3/6}$O$_4$. Meanwhile, when the temperature is greater than 700 °C, an evident increase in the thermal diffusivity of EuNb$_{1-X}$Ta$_X$O$_4$ (X = 0/6, 1/6)

is observed, which is caused by thermal radiation. No obvious increase of thermal diffusivity is detected in EuNb$_{1-X}$Ta$_X$O$_4$ (X = 2/6, 3/6, 4/6), indicating that the B-site substitution of Ta is effective in improving the thermal radiation resistance of EuNbO$_4$. Fig. 5(b) shows that the thermal conductivity (1.52–3.28 W·K^{-1}·m^{-1}, 25–900 °C) of EuNb$_{1-X}$Ta$_X$O$_4$ decreases with an increase in temperature, and that EuNb$_{3/6}$Ta$_{3/6}$O$_4$ exhibits the minimum value (1.52 W·K^{-1}·m^{-1}, 700 °C). The thermal radiation effect causes the thermal conductivity of EuNb$_{1-X}$Ta$_X$O$_4$ (X = 0/6, 1/6, 2/6, 3/6) to increase at high temperatures ($\geq$ 500 °C). No increase in thermal diffusivity or conductivity is detected for EuNb$_{2/6}$Ta$_{4/6}$O$_4$, which is attributed to it having the best thermal radiation resistance.

Thermal transfer is conducted via phonons—that is, lattice vibration—in insulators [28,29]. During phonon propagation, they are scattered via various processes, including Umklapp phonon–phonon scattering, different point defects scattering, grain boundaries scattering, and the other scattering processes [29–32]. The

Table 2
Temperature-dependent specific heat of EuNb$_{1-X}$Ta$_X$O$_4$ (X = 0/6, 1/6, 2/6, 3/6, 4/6) ceramics calculated via the Neumann–Kopp principle.

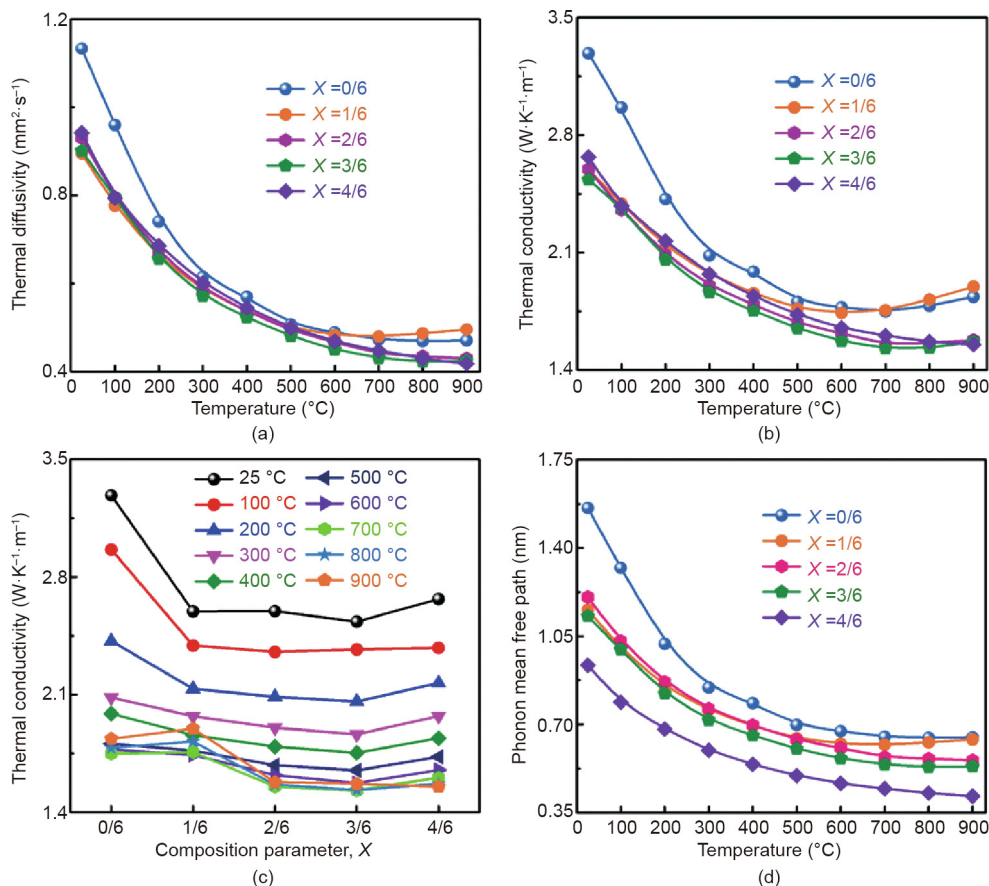| X	Specific heat (J·K^{-1}·g^{-1})									
	25 °C	100 °C	200 °C	300 °C	400 °C	500 °C	600 °C	700 °C	800 °C	900 °C
0/6	0.43	0.46	0.48	0.50	0.52	0.53	0.54	0.55	0.56	0.58
1/6	0.39	0.42	0.44	0.45	0.47	0.48	0.49	0.49	0.51	0.52
2/6	0.37	0.40	0.42	0.44	0.45	0.46	0.47	0.48	0.49	0.50
3/6	0.36	0.38	0.40	0.42	0.43	0.44	0.45	0.46	0.47	0.48
4/6	0.35	0.37	0.39	0.40	0.41	0.42	0.43	0.44	0.45	0.46

Fig. 5. Thermal properties of EuNb$_{1-X}$Ta$_X$O$_4$ (X = 0/6, 1/6, 2/6, 3/6, 4/6) ceramics. (a) Thermal diffusivity; (b) thermal conductivity; (c) composition dependence of thermal conductivity; (d) phonon mean free path.

phonon mean free path (l), which is restricted by the above processes, consists of different parts [29–32]:

$$\frac{1}{l} = \frac{1}{l_p} + \frac{1}{l_d} + \frac{1}{l_b} + \sum_x \frac{1}{l_x} \tag{11}$$

where l_p, l_d, l_b and l_x are the phonon free paths derived from Umklapp phonon–phonon scattering, point defects scattering, grain boundaries scattering, and other processes, respectively [29–32]. Figs. 1 and 2 indicate that no phase transformation is detected, and that the grain size (microscale) is dozens of times greater than the size of phonon free path (nanoscale). Furthermore, the phonon scattering intensity caused by the grain boundary decreases with increase in temperature. Therefore, grain boundaries scattering can not decide the phonon mean free path. According to the chemical formula of $EuNb_{1-X}Ta_XO_4$, no vacancy is induced in $EuNbO_4$ by the B-site substitution of Ta, as both Nb and Ta are pentavalent (+5). The Umklapp scattering degree is reflected via inharmonic lattice vibration. The inharmonic lattice vibration of $EuNbO_4$ is enhanced by the B-site substitution of Ta, and the lowest value of the Grüneisen parameter is detected in $EuNbO_4$ (Table 1). As the Grüneisen parameter increases with an increase in temperature, the thermal conductivity decreases with an increase in temperature. Furthermore, point defects are introduced, which are attributed to the atomic weight difference between Nb (92.9 g·mol^{-1}) and Ta (180.9 g·mol^{-1}). The effective ionic radius of Ta^{5+} and Nb^{5+} with four ligands is equal (0.064 nm); the phonon scattering caused by the ionic radius difference is therefore omitted. Normally, the misfits of atomic weight and ionic radius reach the maximum value when X is 3/6 in the substitution process [25,30,32–34]. Hence, the lowest thermal conductivity of $EuNb_{1-X}Ta_XO_4$ is detected in $EuNb_{3/6}Ta_{3/6}O_4$. The phonon scattering process sketch map of $EuNb_{3/6}Ta_{3/6}O_4$ is displayed in Fig. 6, in which Ta atoms are the strongest phonon scattering sources. First, the B-site substitution of Ta causes an atomic weight difference, as Ta atoms are much heavier than Nb atoms. Second, the introduction of Ta increases the total unit cell weight and crystal structure complexity. The work by Clarke [35] proves that the thermal conductivity decreases with an increase in unit cell weight and crystal structure complexity. Third, the Ta and Nb atoms are centered by four O atoms to form TaO_4 and NbO_4 tetrahedrons. Phonons are scattered via a cage-like structure to reduce the thermal conductivity, which has been reported in various ceramics [32,36,37]. The complex crystal structure and cage-like structure are important reasons why $EuNb_{1-X}Ta_XO_4$ exhibits a low thermal conductivity.

The composition dependence of the thermal conductivity can be clearly observed in Fig. 5(c). At the same temperature, the thermal conductivity of $EuNb_{1-X}Ta_XO_4$ decreases with an increase in Ta content, and increases slightly when X is 4/6. The phonon mean free path (0.41–1.56 nm, 25–900 °C) of $EuNb_{1-X}Ta_XO_4$ decreases with an increase in temperature (Fig. 5(d)). The temperature dependence of l and k is analogous. The lowest l (0.41 nm, 900 °C) was detected in $EuNb_{2/6}Ta_{4/6}O_4$. Eq. (10) indicates that l connects to V_M and λ. V_M is temperature dependent; therefore, the temperature dependence of l is determined by the thermal diffusivity. In addition, V_M of $EuNb_{2/6}Ta_{4/6}O_4$ (3022 m·s^{-1}) is much faster than those of the rest of the samples (2246–2393 m·s^{-1}), which results in the lowest l being detected in $EuNb_{2/6}Ta_{4/6}O_4$.

The thermal radiative conductivity occurs at elevated temperature, and results in an increase of the thermal conductivity. The thermal diffusivity and conductivity, as well as the phonon mean free path, of $EuNb_{1-X}Ta_XO_4$ (X = 0/6, 1/6, 2/6, 3/6) slightly increase at high temperatures. To obtain the intrinsic phonon thermal conductivity of $EuNb_{1-X}Ta_XO_4$, the thermal radiative conductivity should be removed. In the work of Klemens [30] and Ambegaokar [31], the phonon scattering intensity caused by the point defects and grain boundaries is constant, and the mean phonon free path of the insulator predominantly consists of l_p, l_d, and l_b [33–37]. Therefore, the temperature dependence of the thermal diffusivity is decided by the Umklapp phonon–phonon scattering process. The correlation between the temperature T and l_p of crystalline ceramics is as follows [36,37]:

$$l_p = l_0 \left[\exp\left(\bar{T}_D / bT \right) - 1 \right] \tag{12}$$

$$T_D = \frac{h}{k_B} \left(\frac{3m}{4\pi V} \right)^{1/3} V_M \tag{13}$$

$$\bar{T}_D = \frac{T_D}{m^{1/3}} \tag{14}$$

where T_D is the Debye temperature, h is the Plank's constant, k_B is the Boltzmann constant, m is the total weight per unit cell, V is the unit cell volume, l_0 is a parameter before the exponential, $\bar{T}_D$ is the revised Debye temperature, and b is a constant set as 2. When the temperature is greater than $\bar{T}_D$, l is as follows [36,37]:

$$l^{-1} \sim \frac{C}{\exp\left(\frac{T_D}{bTm^{1/3}}\right) - 1} + D = \frac{bCm^{1/3}}{T_D}T + \left(D - \frac{1}{2}C \right) \tag{15}$$

where C and D are parameters. Fig. 5(d) shows that the relationship between l and T clearly deviates from $l \propto T^{-1}$ at elevated temperatures due to the thermal radiation effect. To obtain the intrinsic lattice thermal conductivity of $EuNb_{1-X}Ta_XO_4$, the intrinsic phonon thermal diffusivity should be determined. Based on the relationship between λ and l, λ is determined as follows [36,37]:

$$\lambda^{-1} \sim l^{-1} \sim \frac{bCm^{1/3}}{T_D}T + \left(D - \frac{1}{2}C \right) \tag{16}$$

Eq. (16) indicates that the reciprocal thermal diffusivity increases with an increase in temperature, when no thermal radiation effect occurs. Fig. 7(a) shows that λ^{-1} follows the relationship expressed in Eq. (16) at low temperature. However, when the temperature is greater than 600 °C, λ^{-1} deviates from the $\lambda^{-1} \propto T$ (dotted lines) relationship. The intrinsic phonon thermal diffusivity of $EuNb_{1-X}Ta_XO_4$ is corrected.

Fig. 7(a) shows that the intrinsic phonon thermal diffusivity monotonously decreases with increasing temperature. A similar temperature dependence of the intrinsic phonon thermal conductivity and the phonon mean free path is observed in Figs. 7(c) and 7(d). The minimum intrinsic phonon thermal conductivity of $EuNb_{1-X}Ta_XO_4$ is 1.27 W·K^{-1}·m^{-1} ($EuNb_{3/6}Ta_{3/6}O_4$). The variation trend of the thermal conductivity implies that it will decrease

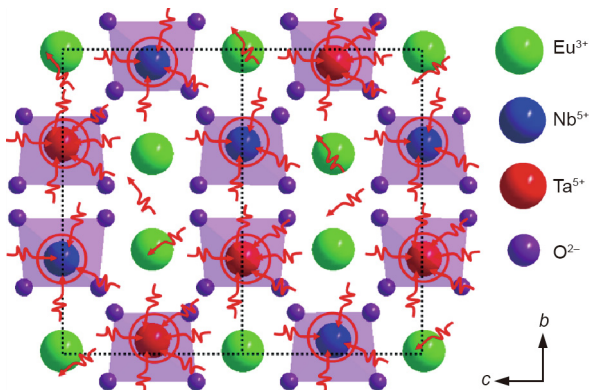**Fig. 6.** Phonon scattering process sketch map of $EuNb_{3/6}Ta_{3/6}O_4$ ceramics viewed from a axis, b and c stand for the rest two axis.

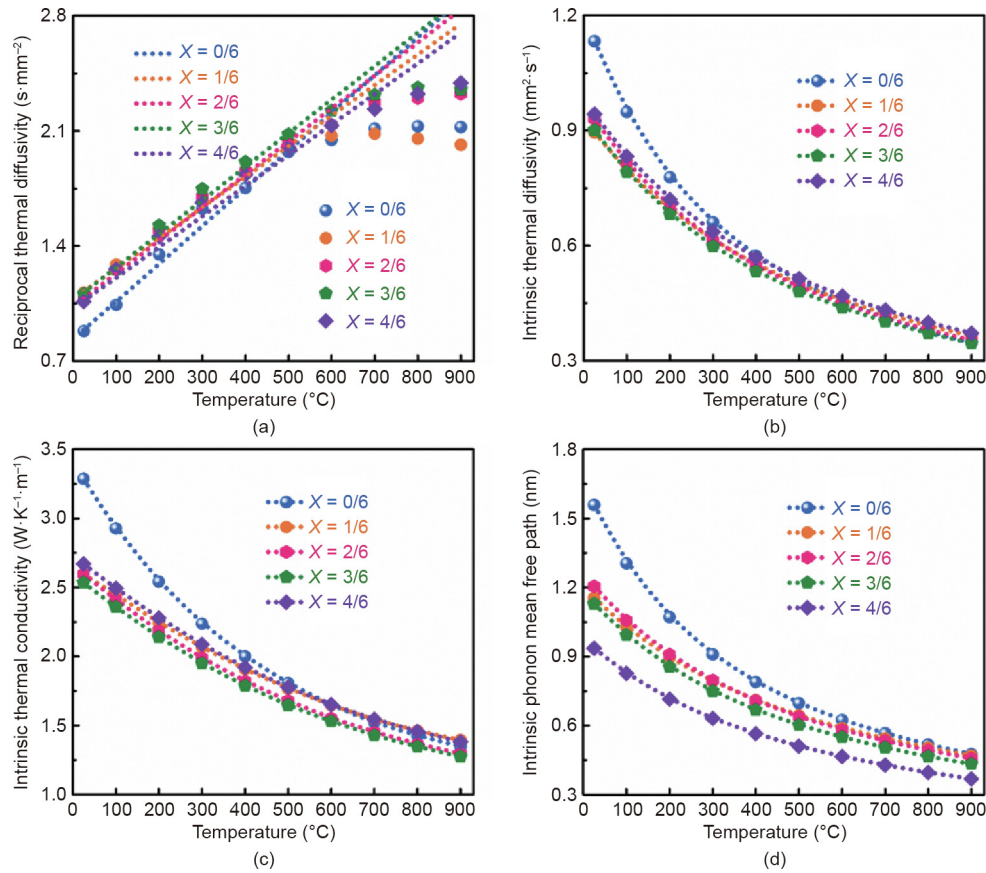**Fig. 7.** Intrinsic thermal properties of EuNb$_{1-X}$Ta$_X$O$_4$ (X = 0/6, 1/6, 2/6, 3/6, 4/6) ceramics. (a) Reciprocal thermal diffusivity; (b) intrinsic phonon thermal diffusivity; (c) intrinsic phonon thermal conductivity; (d) intrinsic phonon mean free path.

further with an increase in temperature, and will approach the theoretical limit value (k_{min}), which has been derived by Cahill et al. [34–36]:

$$k_{min} = \frac{k_B}{2.48} n^{2/3}(2V_T + V_L) \tag{17}$$

where n is the atomic number per unit cell. The theoretical minimum thermal conductivity decreases with a decrease in acoustic velocity. As shown in Table 3, k_{min} of EuNbO$_4$ is about 0.78 W·K^{-1}·m^{-1}, implying that the experimental k of EuNbO$_4$ can be decreased. The ZrO$_2$ alloying effects have been applied to reduce the thermal conductivity of rare earth tantalates, and these methods may be effective for EuNbO$_4$ [38]. Furthermore, the A-site substitution of other rare earth elements (e.g., Gd, Dy, Ho, Yb, Er, and Lu) with a heavier atomic weight can be attempted. As for the thermal radiation effect, dual layer coatings are effective in blocking the thermal radiative conductivity of LaPO$_4$/La$_2$Zr$_2$O$_7$ ceramics [39]. EuPO$_4$/EuNbO$_4$ dual coatings can be used to attempt to reduce the thermal radiative conductivity of EuNbO$_4$, due to the excellent thermal radiation resistance of rare earth phosphate (REPO$_4$) [40].

4. Conclusion

The thermal and mechanical properties of EuNbO$_4$ synthesized via a SSR have been successfully optimized by the B-site substitution of Ta. The highest TEC reaches 11.2 × 10^{-6} K^{-1} at 1200 °C (EuNb$_{3/6}$Ta$_{3/6}$O$_4$), attributed to crystal structure relaxation and the enhancement of inharmonic lattice vibration strength. The highest Young's modulus (169 GPa) is detected in EuNb$_{2/6}$Ta$_{4/6}$O$_4$, as the Ta–O bond strength is much greater than that of the Nb–O bond. The minimum experimental thermal conductivity (1.52 W·K^{-1}·m^{-1}, 700 °C) is found in EuNb$_{3/6}$Ta$_{3/6}$O$_4$, due to the maximum misfit of atomic weight between Ta and Nb. The thermal radiation resistance of EuNb$_{1-X}$Ta$_X$O$_4$ is improved via the B-site substitution of Ta. The theoretical minimum thermal conductivity (0.78 W·K^{-1}·m^{-1}) of EuNbO$_4$ indicates that the experimental thermal conductivity can be reduced further. It is clear that EuNb$_{1-X}$Ta$_X$O$_4$ exhibits lower thermal conductivity, lower Young's modulus and greater TECs than the 7YSZ and La$_2$Zr$_2$O$_7$ ceramics. The excellent material properties of EuNb$_{1-X}$Ta$_X$O$_4$ imply that EuNbO$_4$ is a promising high-temperature TBC.

Table 3
Fitted reciprocal thermal diffusivity (λ^{-1}) and theoretical minimum thermal conductivity (k_{min}) of EuNb$_{1-X}$Ta$_X$O$_4$ (X = 0/6, 1/6, 2/6, 3/6, 4/6) ceramics.

X	Intrinsic λ^{-1} (s·m^{-2})	C	D	k_{min} (W·K^{-1}·m^{-1})
0/6	2 290T + 198 923	30 590	214 218	0.78
1/6	1 858T + 563 551	25 248	576 176	0.87
2/6	2 006T + 477 306	26 762	490 687	0.89
3/6	2 040T + 501 880	27 736	515 748	0.87
4/6	1 859T + 506 708	31 505	522 461	1.05

Compliance with ethics guidelines

Lin Chen and Jing Feng declare that they have no conflict of interest or financial conflicts to disclose.

References

[1] Wang J, Chong XY, Zhou R, Feng J. Microstructure and thermal properties of RETaO$_4$ (RE = Nd, Eu, Gd, Dy, Er, Yb, Lu) as promising thermal barrier coating materials. Scr Mater 2017;126:24–8.

[2] Sarin P, Hughes RW, Lowry DR, Apostolov ZD, Kriven WM. High-temperature properties and ferroelastic phase transition in rare earth niobates (LnNbO$_4$). J Am Ceram Soc 2014;97(10):3307–19.

[3] Brixner LH, Whitney JF, Zumsteg FC, Jones GA. Ferroelasticity in the LnNbO$_4$-type rare earth niobates. Mater Res Bull 1977;12(1):17–24.

[4] Machida M, Murakami S, Kijima T. Photocatalytic property and electronic structure of lanthanide tantalates, LnTaO$_4$ (Ln = La, Ce, Pr, Nd and Sm). J Phys Chem B 2001;105(16):3289–94.

[5] Haugsrud R, Norby T. Proton conduction in rare-earth ortho-niobates and ortho-tantalates. Nat Mater 2006;5(3):193–6.

[6] Kim DW, Kwon DK, Yoon SH, Hong KS. Microwave dielectric properties of rare-earth ortho-niobates with ferroelasticity. J Am Ceram Soc 2006;89(12):3861–4.

[7] Jian L, Wayman CM. Compressive behavior and domain-related shape memory effect in LaNbO$_4$ ceramics. Mater Lett 1996;26(1–2):1–7.

[8] Feng J, Shian S, Xiao B, Clarke DR. First-principles calculations of the high-temperature phase transformation in yttrium tantalate. Phys Rev B 2014;90(9):094102.

[9] Mercer C, Williams JR, Clarke DR, Evans AG. On a ferroelastic mechanism governing the toughness of metastable tetragonal-prime (*t'*) yttria-stabilized zirconia. Proc R Soc A 2007;463(2081):1393–408.

[10] Li GR, Wang LS. Durable TBCs with self-enhanced thermal insulation based on co-design on macro- and microstructure. Appl Surf Sci 2019;483:472–80.

[11] Ren XR, Pan W. Mechanical properties of high-temperature-degraded yttria-stabilized zirconia. Acta Mater 2014;69:397–406.

[12] Li QL, Song P, Lü KY, Dong Q, Li Q, Tan J, et al. Fracture behaviour of ceramic–metallic glass gradient transition coating. Ceram Int 2019;45(5):5566–76.

[13] Liu MJ, Zhang M, Zhang XF, Li GR, Zhang Q, Li CX, et al. Transport and deposition behaviors of vapor coating materials in plasma spray-physical vapor deposition. Appl Surf Sci 2019;486:80–92.

[14] Liu YC, Liu B, Xiang HM, Zhou YC, Nian HQ, Chen HF, et al. Theoretical investigation of anisotropic mechanical and thermal properties of *A*BO$_3$ (*A* = Sr, Ba; *B* = Ti, Zr, Hf) perovskites. J Am Ceram Soc 2018;101(8):3527–40.

[15] Liu B, Wang JY, Li FZ, Zhou YC. Theoretical elastic stiffness, structural stability and thermal conductivity of La$_2$T$_2$O$_7$ (*T* = Ge, Ti, Sn, Zr, Hf) pyrochlore. Acta Mater 2010;58(13):4369–77.

[16] Chen L, Jiang YH, Chong XY, Feng J. Synthesis and thermophysical properties of RETa$_3$O$_9$ (RE = Ce, Nd, Sm, Eu, Gd, Dy, Er) as promising thermal barrier coatings. J Am Ceram Soc 2018;101(13):1266–78.

[17] Liu MJ, Zhang KJ, Zhang Q, Zhang M, Yang GJ, Li CX, et al. Thermodynamic conditions for cluster formation in supersaturated boundary layer during plasma spray-physical vapor deposition. Appl Surf Sci 2019;471:950–9.

[18] Song XM, Meng FL, Kong MG, Liu ZW, Huang LP, Zheng XB, et al. Relationship between cracks and microstructures in APS YSZ coatings at elevated temperatures. Mater Character 2017;131:277–84.

[19] Li GR, Li G, Wang L, Yang G. A novel composite-layered coating enabling self-enhancing thermal barrier performance. Scr Mater 2019;163:142–7.

[20] Sanditov DS, Belomestnykh VN. Relation between the parameters of the elasticity theory and averaged bulk modulus of solids. Tech Phys 2011;56(11):1619–23.

[21] Schlichting KW, Padture NP, Klemens PG. Thermal conductivity of dense and porous yttria-stabilized zirconia. J Mater Sci 2001;36(12):3003–10.

[22] Leitner J, Chuchvalec P, Sedmidubsky D, Strejc A, Abrman P. Estimation of heat capacities of solid mixed oxides. Thermochim Acta 2003;395(1–2):27–46.

[23] Kittle C. Introduction to solid state physics. 6th ed. New York: John Wiley & Sons; 1986.

[24] Feng J, Xiao B, Zhou R, Pan W. Anisotropy in elasticity and thermal conductivity of monazite-type REPO$_4$ (RE = La, Ce, Nd, Sm, Eu and Gd) from first-principles calculations. Acta Mater 2013;61(19):7364–83.

[25] Zhao M, Pan W, Wan CL, Qu ZX, Li Z, Yang J. Defect engineering in development of low thermal conductivity materials: a review. J Eur Ceram Soc 2016;37(1):1–13.

[26] Zhao M, Ren XR, Pan W. Mechanical and thermal properties of simultaneously substituted pyrochlore compounds (Ca$_2$Nb$_2$O$_7$)$_x$(Gd$_2$Zr$_2$O$_7$)$_{1-x}$. J Eur Ceram Soc 2015;35(3):1055–61.

[27] Li QL, Song P, He X, Yu X, Li C, Huang TH, et al. Plastic metallic-barrier layer for crack propagation within plasma-sprayed Cu/ceramic coatings. Surf Coat Tech 2019;360(25):259–68.

[28] Slack GA. The thermal conductivity of nonmetallic crystals. Solid State Phys 1979;34:1–71.

[29] Ge ZH, Ji YH, Qiu Y, Chong XY, Feng J, He JQ. Enhanced thermoelectric properties of bismuth telluride bulk achieved by telluride-spilling during the spark plasma sintering process. Scr Mater 2018;143:90–3.

[30] Klemens PG. Thermal resistance due to point defects at high temperatures. Phys Rev 1960;119(2):507–9.

[31] Ambegaokar V. Thermal resistance due to isotopes at high temperatures. Phys Rev 1959;114(2):488–9.

[32] Wan CL, Pan W, Xu Q, Qin YX, Wang JD, Qu ZX, et al. Effect of point defects on the thermal transport properties of (La$_x$Gd$_{1-x}$)$_2$Zr$_2$O$_7$: experiment and theoretical model. Phys Rev B 2006;74:144109.

[33] Raychaudhuri AK. Origin of the plateau in the low-temperature thermal conductivity of silica. Phys Rev B Condens Matter 1989;39(3):1927–31.

[34] Cahill DG, Watson SK, Pohl RO. Lower limit to the thermal conductivity of disordered crystals. Phys Rev B Condens Matter 1992;46(10):6131–40.

[35] Clarke DR. Materials selection guidelines for low thermal conductivity thermal barrier coatings. Surf Coat Tech 2003;163–4:67–74.

[36] Tian ZL, Sun LC, Wang JM, Wang JY. Theoretical prediction and experimental determination of the low lattice thermal conductivity of Lu$_2$SiO$_5$. J Eur Ceram Soc 2015;35(6):1923–32.

[37] Bruls RJ, Hintzen HT, Metselaar R. A new estimation method for the intrinsic thermal conductivity of nonmetallic compounds: a case study for MgSiN$_2$, AlN and Si$_3$N$_4$ ceramics. J Eur Ceram Soc 2005;25(6):767–79.

[38] Chen L, Song P, Feng J. Influence of ZrO$_2$ alloying effect on the thermophysical properties of fluorite-type Eu$_3$TaO$_7$ ceramics. Scr Mater 2018;152:117–21.

[39] Yang J, Wan CL, Zhao M, Shahid M, Pan W. Effective blocking of radiative thermal conductivity in La$_2$Zr$_2$O$_7$/LaPO$_4$ composites for high temperature thermal insulation applications. J Eur Ceram Soc 2016;36(15):3809–14.

[40] Du AB, Wan CL, Qu ZX, Pan W. Thermal conductivity of monazite-type REPO$_4$ (RE = La, Ce, Nd, Sm, Eu, Gd). J Am Ceram Soc 2009;92(11):2687–92.